Composite Structures 311 (2023) 116807

Contents lists available at ScienceDirect

Composite Structures

journal homepage: www.elsevier.com/locate/compstruct

# Topology optimization with graded infill accounting for loading uncertainty

Matteo Bruggi [a,*], Hussein Ismail [a,b], János Lógó [b]

[a] Department of Civil and Environmental Engineering, Politecnico di Milano, Italy
[b] Department of Structural Mechanics, Budapest University of Technology and Economics, Hungary

ARTICLE INFO

*Keywords:*
Homogenization
Robust topology optimization
Probabilistic loads
Coated structures
Additive manufacturing

ABSTRACT

The optimal design of composite structures made of a solid phase and a given fraction of graded infill is addressed, using homogenization-based topology optimization and accounting for uncertainty in loading amplitude. A two-phase material law with void is implemented to control the amount of graded infill to be distributed, along with its admissible density range. Numerical homogenization is used to derive the macroscopic elastic properties of an isotropic and two orthotropic infills that are commonly used in additive manufacturing. A minimum weight problem is endowed with a set of deterministic displacement constraints that are equivalent to stochastic displacement enforcements in case of normal distributions of the amplitude of the applied forces. Sequential convex programming is adopted to solve the arising multi-constrained problem. Numerical simulations are performed to assess the proposed algorithm and point out peculiar features of the achieved optimal solutions with respect to layouts found in case of deterministic loads. When a fraction of graded infill is prescribed, coated structures are retrieved, whose shape may be remarkably affected by the selected type of lattice.

## 1. Introduction

Topology optimization is a well-known design tool that searches a given domain for the optimal distribution of material to meet prescribed goals and requirements, see [1] and [2]. Upon introduction of a so-called "density" field, a suitable interpolation law may be adopted to penalize the constitutive properties of the material, such that a constrained minimization problem may be formulated in terms of the unknown field. A strong penalization of the intermediate values of the density is operated through the Solid Isotropic Material with Penalization (SIMP) [3], which was conceived to achieve optimal layouts made of a void fraction ("0" or "white") and a solid one ("1" or "black"). Alternatively, intermediate density regions ("gray") may be admitted. This allows to circumvent the ill-posedness of the continuous problem that distributes "void" and solid phase only, see in particular [4], and to address the design of composite structures, see the recent and comprehensive review on multi-scale topology optimization in [5]. A procedure of inverse homogenization, see e.g. [6–9], may be required to derive the shape of the microstructures corresponding to intermediate values of the unknown density field. When multiple patterns are generated, see e.g. [10], a typical issue is that different patches cannot be easily connected altogether. Undesired geometrical singularities are expected, unless this has been explicitly accounted for in the formulation, see e.g. [11–13]. Alternatively, one may use topology optimization to distribute a graded microstructure of a given shape, see e.g. [14,15]. Assuming a separation of scales, asymptotic homogenization [16,17] can be employed to compute the effective elastic properties of a lattice material as a function of one or more design unknowns, i.e. one or more geometrical parameters governing the material law of a microstructure to be graded within the design domain, see e.g. [18,19].

Additive manufacturing (AM) remarkably reduces restrictions imposed by conventional subtractive manufacturing techniques when fabricating optimal layouts, see in particular [20–22]. Indeed, lattice structures can be used to build lightweight infills that are often preferred over solid interiors especially when using 3d-printing [23]. Reference is also made to the optimal design of sandwich structures, in which both the thickness and the location of the coating are generally prescribed, see e.g. [24–28]. Selective Laser Sintering (SLS) benefits from porous infills of any given shape, whereas the layer–by–layer process peculiar to Fused Deposition Modelling (FDM) requires layouts with a limited overhang. For angles exceeding 45° degrees with respect to the printing direction the previous layers are generally not sufficient to build upon safely, calling for additional supports, see e.g. [29]. Self-supporting lattices are extensively used to solve overhang issues as an alternative to the adoption of printing supports for blueprints with given shape, see in particular [30].

* Corresponding author.
*E-mail addresses:* matteo.bruggi@polimi.it (M. Bruggi), hussein.ismail@emk.bme.hu, hussein.ismail@polimi.it (H. Ismail), logo.janos@emk.bme.hu (J. Lógó).

https://doi.org/10.1016/j.compstruct.2023.116807
Received 7 July 2022; Received in revised form 29 December 2022; Accepted 11 February 2023
Available online 15 February 2023

The inherent uncertainty related to load, geometry and mechanical parameters affects engineering applications. The above mentioned sources of uncertainty have been originally taken into account in truss design, see [31] and [32]. Concerning topology optimization, a few main approaches exist, see [33]. In reliability–based optimization, limit states are defined and their probability of failure is addressed. Marginal probability density functions of the random variables representing the uncertainties must be known, see e.g. [34]. In the so–called robust design methods, first- and second- order stochastic moments of the system response are considered, see e.g. [35]. The latter approach has been used for random loads e.g. in [36–38] for compliant structures, and in [39] for compliant mechanisms. Reference is also made to [40,41] for extended discussions on the methods available to cope with geometric and material uncertainties. Besides, non–probabilistic approaches have been developed to deal with cases in which only the bounds of the uncertain variables are available, see [42] and [43].

It must be remarked that only a few investigations are available in the literature considering load uncertainly in topology optimization with multiple material phases. In [44], robust multi-material structures under interval loading uncertainty are designed by combining orthogonal decomposition with uniform sampling, whereas [45] takes advantage of an alternating active-phase method to minimize a weighted sum of the mean and standard deviation of the structural compliance. In both cases, the strain energy at equilibrium is the objective function to be minimized, whereas the weight of each solid phase, or the available amount of material, is prescribed. No porous structure is allowed in the final design. The arising volume-constrained optimization is solved using evolutionary methods and optimality criteria, in [44] and [45] respectively.

Within the above framework, this contribution addresses the minimum weight design of composite structures made of a solid phase and a graded infill. Instead of working with the strain energy as a global measure of the overall stiffness, local displacement constraints are implemented, accounting for uncertainty in loading amplitude. A failure probability may be prescribed for each of them, combining homogenization and topology optimization to formulate a design problem that can be efficiently solved by mathematical programming. According to [46], the work in [36] showed that a probabilistic constraint on the structural compliance can be replaced by an equivalent deterministic one if the uncertainty in the load amplitude can be described by a joint normal distribution function. In this contribution it is shown that the original theory given in [46] can be straightforwardly applied to displacement constraints when addressing any linear elastic structure subjected to a set of point forces that are affected by the same type of uncertainty. This allows to prescribe an accepted failure probability for any displacement constraint that is enforced when dealing with the design of a composite structure at the serviceability limit state [47]. Numerical homogenization is used to derive the macroscopic elastic properties of any orthotropic infill to be graded in the optimal solution. A two-phase material law with void is implemented to distribute the solid phase while controlling the amount of graded infill used in the solution. The proposed material law is conceived to achieve full separation of the phases and control effectively the admissible density range of the graded infill. Indeed, the arising multi-constrained formulation is endowed with an additional enforcement governing the minimum weight of the porous phase. Sequential convex programming is used to perform the optimization, see [48].

When disregarding the constraint on the amount of graded porous microstructure, minimum weight layouts that consist only of full material (and void) are found. Partially constrained layouts that may arise among statically determinate solutions for deterministic loads are replaced by completely constrained ones when introducing uncertainties in the optimization. By enforcing a minimum amount of porous phase, the proposed probabilistic approach retrieves optimal solutions consisting of a solid coating that partially or fully encloses one or more regions of infill. An isotropic lattice with high stiffness-to-weight ratio is considered, as well as two self-supporting orthotropic infills. Numerical simulations show that the selected type of lattice remarkably affects the topology of the optimal results, including thickness and locations of the solid features. According to the achieved results, the adopted formulation may be used to generate coated structures which are feasible with respect to the prescribed accepted failure probability of the local displacement constraints and may be effectively manufactured using 3d-printing techniques.

The paper is organized as follows. In Section 2 the homogenized elastic properties of the considered isotropic and orthotropic infills are discussed, the two-phase material law is presented, and the derivation of the probabilistic displacement constraints is given for the proposed homogenization-based formulation of topology optimization. Numerical simulations are presented in Section 3, investigating different assumption in terms of the correlation of the considered uncertain loading and different optimization parameters. Section 4 resumes the main findings of this contribution, outlining ongoing extensions. In particular, it is remarked that the proposed approach can be straightforwardly extended to stress-constrained problems in which an accepted failure probability of local enforcements on material strength has to be prescribed.

## 2. Method

### 2.1. A two-phase material model with void

A two-phase interpolation law is adopted to distribute full material and void, along with a fraction of a porous graded microstructure with prescribed layout. Assuming plane stress conditions, the Cartesian components of the macroscopic stress tensor $\sigma_{ij}$ are gathered in the array $\underline{\sigma} = [\sigma_{11}\ \sigma_{22}\ \sigma_{12}]^T$ and, analogously, $\underline{\varepsilon} = [\varepsilon_{11}\ \varepsilon_{22}\ \gamma_{12}]^T$ for the in plane components of the macroscopic strain tensor $\varepsilon_{ij}$. The constitutive law for the herein considered linear elastic material reads $\underline{\sigma} = \mathbf{C}\underline{\varepsilon}$, where:

$$\mathbf{C}(\rho_1, \rho_2, \rho_g) = \mathbf{C}_{min} + \rho_1^p(\mathbf{C}_0 - \mathbf{C}_{min}) + \rho_2^p(1-\rho_1^p)\left(\mathbf{C}_H(\rho_g) - \mathbf{C}_{min}\right), \qquad (1)$$

with penalization $p \geq 3$. In the above equation, $0 \leq \rho_1, \rho_2 \leq 1$ and $\rho_{g,min} \leq \rho_g \leq \rho_{g,max}$ are three variables governing the material law, being $\rho_{g,min}$ and $\rho_{g,max}$ the bounds of the admissible density range of the porous phase. For $\rho_1 = 1$, whatever the value of $\rho_2$ and $\rho_g$, the constitutive matrix is that of full material, i.e. $\mathbf{C}_0$. For $\rho_1 = \rho_2 = 0$, independently on the value of $\rho_g$, only the terms $C_{min}$ survives, meaning that a fictitious stiffness that stands for void is found. For $\rho_1 = 0$ and $\rho_2 = 1$, a porous microstructure may arise with a macroscopic stiffness tensor $\mathbf{C}_H$ that depends on the density of the porous phase $\rho_g$, according to the following interpolation:

$$\mathbf{C}_H = \begin{bmatrix} c_{H,11}(\rho_g)C_{0,11} & c_{H,12}(\rho_g)C_{0,12} & 0 \\ & c_{H,22}(\rho_g)C_{0,22} & 0 \\ sym & & c_{H,33}(\rho_g)C_{0,33} \end{bmatrix}. \qquad (2)$$

In the above equation, $C_{0,ij}$ are the entries of $\mathbf{C}_0$ and $0 \leq c_{H,ij} \leq 1$. It is also remarked that, for $\rho_2 = 1$, either graded or full material arises depending on the value of $\rho_1$, but void is not allowed. This will be exploited in Section 3.

In Eq. (1), the so-called Solid Isotropic Material with Penalization is used, see in particular [1,3,49]. The penalization of $\rho_1$ and $\rho_2$ steers the design towards its limit values, i.e. $\rho_1 = 1$ (full material) or $\rho_1 = 0$ (void or porous microstructure graded by $\rho_g$, for $\rho_2 = 0$ and $\rho_2 = 1$ respectively), see in particular discussions on multi-material laws in [50,51]. In the numerical simulations, $p$ is smoothly increased from 3 to 6 through a continuation approach, see e.g. [52].

The dependence of the macroscopic stress–strain matrix $\mathbf{C}_H$ on the density of the porous phase $\rho_g$ is evaluated by performing numerical homogenization on the base cells represented in Fig. 1, see in particular [53]. An hexagonal close-packing of circular holes (HCP), a diamond lattice (D), and an elongated diamond lattice (E), are considered in the

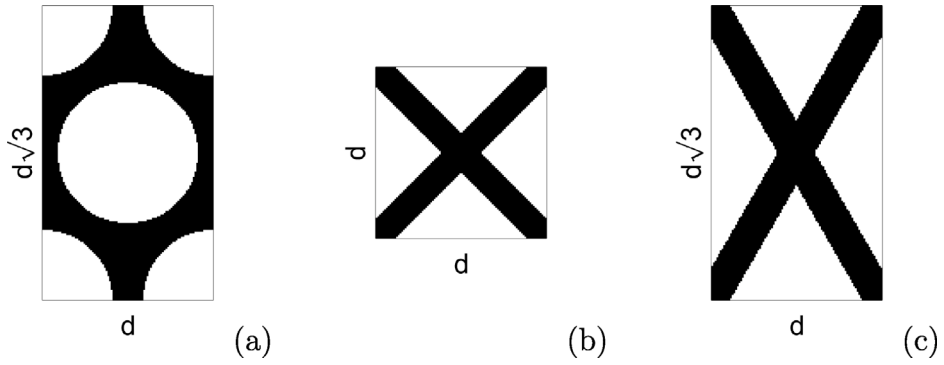


**Fig. 1.** Base cells used in the numerical studies (for $\rho_g = 0.40$): hexagonal close-packing of circular holes (HCP) (a), diamond lattice (D) (b), elongated diamond lattice (E) (c).

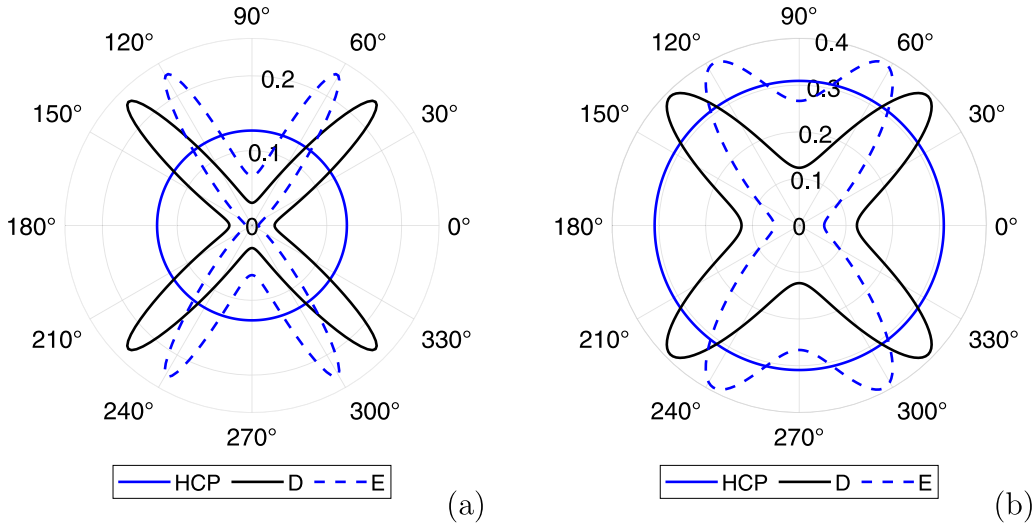


**Fig. 2.** Apparent Young's modulus of the hexagonal close-packing of circular holes (HCP), diamond lattice (D) and elongated diamond lattice (E), at $\rho_g = 0.40$ (a) and $\rho_g = 0.60$ (b), depending on the orientation of the reference system. Values are scaled with respect to that of the full isotropic material phase.

**Table 1**
Interpolation law of the type $\alpha_i x^i$, with $i = 1, 2, \ldots, 5$, for the components of the macroscopic stiffness tensor given in Eq. (2), as computed for an hexagonal close-packing of circular holes (HCP), a diamond lattice (D) and an elongated diamond lattice (E), using numerical homogenization.

| | | $\alpha_5$ | $\alpha_4$ | $\alpha_3$ | $\alpha_2$ | $\alpha_1$ |
|---|---|---|---|---|---|---|
| HCP | $c_{H,11}$ | 1.8839 | −3.3427 | 2.2047 | 0.0887 | 0.1655 |
| | $c_{H,22}$ | 1.8839 | −3.3427 | 2.2047 | 0.0887 | 0.1655 |
| | $c_{H,12}$ | −1.3821 | 5.3524 | −5.2365 | 1.8771 | 0.3890 |
| | $c_{H,33}$ | 3.5169 | −7.6903 | 5.9253 | −0.8056 | 0.0537 |
| D | $c_{H,11}$ | 0.2658 | 1.0553 | −1.0613 | 0.5657 | 0.1745 |
| | $c_{H,22}$ | 0.2658 | 1.0553 | −1.0613 | 0.5657 | 0.1745 |
| | $c_{H,12}$ | 7.1616 | −15.3504 | 11.0124 | −2.7829 | 0.9592 |
| | $c_{H,33}$ | 2.9682 | −5.8757 | 4.2530 | −1.1244 | 0.7788 |
| E | $c_{H,11}$ | 3.1347 | −3.4690 | 1.4453 | −0.1698 | 0.0588 |
| | $c_{H,22}$ | 1.3045 | −2.2048 | 1.5097 | −0.1068 | 0.4974 |
| | $c_{H,12}$ | 5.9369 | −10.3534 | 5.9877 | −1.1476 | 0.5764 |
| | $c_{H,33}$ | 3.2259 | −5.9110 | 3.9148 | −0.7816 | 0.5520 |

numerical studies, being $d$ the reference dimension of the microstructure. For the sake of simplicity, unitary Young's modulus and Poisson's ratio equal to $1/3$ are assumed. The pixel-based method implemented in [54] is used addressing a regular mesh with pixel dimension $l_{pix} = d/100$ and values of the material density in the interval $0.15 - 1$. A fifth degree polynomial, for which zero stiffness is additionally enforced at $\rho_g = 0$, is used to fit the achieved results. It is well-known that the HCP microstructure is isotropic [55], whereas both the D and E lattices are orthotropic [56], see results in Table 1.

Fig. 2 shows polar diagrams of the apparent Young's modulus of the considered porous microstructures for two different values of $\rho_g$, namely:

$$\frac{1}{E} = \frac{1}{E_1}c^4 + \left(\frac{1}{G_{12}} - 2\frac{\nu_{12}}{E_1}\right)s^2c^2 + \frac{1}{E_2}s^4, \tag{3}$$

for $\rho_g = 0.40$ and $\rho_g = 0.60$. Eq. (3) gives the apparent value of the Young's modulus at the orientation $\theta$ from the horizontal direction, being $c = \cos\theta$ and $s = \sin\theta$, $E_1$ and $E_2$ the macroscopic Young's moduli along the horizontal and the vertical direction, respectively, $\nu_{12}$ and $\nu_{21}$ the Poisson's ratios (with $\nu_{12}E_2 = \nu_{21}E_1$), and $G_{12}$ the macroscopic shear modulus, i.e.:

$$\begin{aligned} &\nu_{12} = \frac{C_{H,12}}{C_{H,22}}, \quad \nu_{21} = \frac{C_{H,12}}{C_{H,11}}, \quad G_{12} = C_{H,33}, \\ &E_{11} = C_{H,11}(1 - \nu_{12}\nu_{21}), \quad E_{22} = C_{H,22}(1 - \nu_{12}\nu_{21}), \end{aligned} \tag{4}$$

see e.g. [57].

For $\rho_g = 0.40$, the stiffest directions of the diamond infill and of the elongated diamond infill are characterized by an apparent elastic modulus that is almost twice than for the isotropic microstructure. Very small values of the elastic modulus are attained a few degree far away from these directions. For $\rho_g = 0.60$, the difference in terms of maximum stiffness decreases, but the weakest directions of the diamond infill and the horizontal direction of the elongated diamond infill are still characterized by low values of the elastic modulus. Due to the strong anisotropy of the rhombic cells, non-trivial distributions of the infill are expected when looking for optimal distribution of materials through Eq. (1), see also [58].

### 2.2. Formulation

A finite element discretization of a given design domain is operated, using four-node displacement-based plane stress elements. Three sets of element-wise design variables are considered to implement the linear elastic material law of Eq. (1). In the $e$th of the $n_e$ elements of the mesh, $\rho_{1,e}$, $\rho_{2,e}$ and $\rho_{g,e}$ are the discrete counterpart of the unknown fields $\rho_1$, $\rho_2$ and $\rho_g$, respectively.

A set of $l$ probabilistic point loads acting simultaneously is considered. The intensity of the $j$–th force $f_j$ is a random variable with normal (Gaussian) distribution and mean value $\bar{f}_j$. The covariance matrix is denoted as $\mathbf{K}_{ov}$, whose components are $k_{a,b}$. In case of uncorrelated loads, $\mathbf{K}_{ov}$ is a diagonal matrix whose terms are the variances of the random variables, i.e. $k_{a,a} = \sigma_a^2$, being $\sigma_a$ the standard deviation of the intensity of the $a$–th force $f_a$. It is recalled that $\sigma_a = CV_a \bar{f}_a$, where $CV_a$ is the coefficient of variation of $f_a$. If the loads are correlated, off-diagonal terms arise to account for the (non–zero) covariances, i.e. $k_{a,b} = \sigma_{a,b} = r_{ab}\sigma_a\sigma_b$, being $-1 \le r_{ab} \le 1$ the correlation between the intensity of the $a$–th force $f_a$ and that of the $b$–th force $f_b$.

A problem for the design of a topology of minimum weight under displacement constraints can be stated as:

$$\begin{cases} \min\limits_{\substack{0\le\rho_{1,e},\rho_{2,e}\le 1\\ \rho_{g,min}\le\rho_{g,e}\le\rho_{g,max}}} W = \sum\limits_{e=1}^{n}\left(\rho_{1,e} + (1-\rho_{1,e})\rho_{2,e}\rho_{g,e}\right) W_{0,e} & \text{(a)} \\ \text{s.t.} \quad \mathbf{K}(\boldsymbol{\rho_1},\boldsymbol{\rho_2},\boldsymbol{\rho_g})\,\mathbf{U}_j^{unit} = \mathbf{F}_j^{unit}, \quad \text{for} \quad j = 1...l, & \text{(b)} \\ P(u_i \le u_{lim,i}) \ge 1 - P_{fail}, \quad \text{for} \quad i = 1...m, & \text{(c)} \\ \sum\limits_{e=1}^{n}(1-\rho_{1,e})\rho_{2,e}\rho_{g,e}\,W_{0,e} \ge w_f \sum\limits_{e=1}^{n} W_{0,e}. & \text{(d)} \end{cases} \tag{5}$$

In the above statement, the objective function is the weight of the component, which is computed through the sum of the element contributions $(\rho_{1,e} + (1-\rho_{1,e})\rho_{2,e}\rho_{g,e})\,W_{0,e}$, being $W_{0,e}$ the volume of the $e$th element for $\rho_e = 1$. In this sum, the first term addresses full material, whereas the second the graded one.

Eq. (5b) prescribes the discrete elastic equilibrium. The global stiffness matrix $\mathbf{K}(\boldsymbol{\rho_1},\boldsymbol{\rho_2},\boldsymbol{\rho_g})$ is computed by assembling the element contributions that account for the constitutive law given in Eq. (1). Each of them may be conveniently written accounting separately for the contributions that depends on the interpolation of the terms $C_{H,11}$, $C_{H,12}$, $C_{H,22}$, $C_{H,33}$ in Eq. (2). For the $j$th of the $l$ forces acting simultaneously on the domain, $\mathbf{F}_j^{unit}$ is the load vector that refers to a unit force with same point of application and direction of $f_j$, and $\mathbf{U}_j^{unit}$ is the corresponding nodal displacement vector.

The $i$th of the $m$ displacement components to be controlled is denoted by $u_i$. Eq. (5c) enforces the probability that $u_i$ does not exceed $u_{lim,i}$ to be at least equal to a prescribed value $1-P_{fail}$, being $u_{lim,i}$ for the relevant maximum displacement allowed and $P_{fail}$ the accepted failure probability, see [47]. By exploiting superposition of effects, valid in the considered linear setting, the displacement $u_i$ may be computed as the sum of the (deterministic) displacements $u_{i,j}^{unit}$ due to the forces $\mathbf{F}_j^{unit}$, scaled by the (probabilistic) magnitude $f_j$, i.e.:

$$u_i = \sum_{j=1}^{l} \mathbf{L}_i^T \mathbf{U}_j^{unit} f_j = \sum_{j=1}^{l} u_{i,j}^{unit} f_j, \tag{6}$$

where $\mathbf{L}_i$ is a vector made of zeros except for the entry referring to the $i$th displacement degree of freedom, which takes unitary value.

According to [46], if $\xi_1, \xi_2, \dots, \xi_s$ have a joint normal distribution, then the vector $\mathbf{x} \in \mathbb{R}^s$ with components $x_1, x_2, \dots, x_s$ satisfying:

$$P\left(\sum_{h=1}^{s} x_r \xi_r \le 0\right) \ge q, \tag{7}$$

is the same as that satisfying:

$$\sum_{h=1}^{s} x_h \bar{\xi}_h + \boldsymbol{\Phi}^{-1}(q)\left(\mathbf{x}^T \mathbf{K}_{ov} \mathbf{x}\right)^{1/2} \le 0, \tag{8}$$

where $\bar{\xi}_h$ is the mean value of $\xi_h$, $\mathbf{K}_{ov}$ is the covariance matrix of the random vector $\boldsymbol{\xi}$, and $\boldsymbol{\Phi}^{-1}(q)$ is the inverse cumulative distribution function of the normal distribution (probit function), evaluated at the prescribed probability $q$.

Exploiting Eq. (6), the probabilistic constraint of Eq. (5c) may be re-written in the form:

$$P\left(\sum_{j=1}^{l} u_{i,j}^{unit} f_j - u_{lim,i} \le 0\right) \ge 1 - P_{fail}. \tag{9}$$

According to Eqs. (7)–(8), since it has been assumed that $f_1, f_2, \dots, f_l$ have a joint normal distribution, then the vector $\mathbf{u}_i^{unit}$ with components $u_{i,1}^{unit}, u_{i,2}^{unit}, \dots, u_{i,l}^{unit}$ satisfying Eq. (9) is the same as that satisfying:

$$\sum_{j=1}^{l} u_{i,j}^{unit} \bar{f}_j + \boldsymbol{\Phi}^{-1}(1-P_{fail})\left((\mathbf{u}_i^{unit})^T \mathbf{K}_{ov} \mathbf{u}_i^{unit}\right)^{1/2} - u_{lim,i} \le 0, \tag{10}$$

where $-u_{lim,i}$ of Eq. (9) may be straightforwardly handled through Eqs. (7)–(8) by introducing the slack variables $x_{s+1} = -1$ and $\xi_{s+1} = u_{lim,i}$, the latter with zero variance and zero covariance, see [36].

The above deterministic inequality will be implemented in Eq. (5), instead of the original probability constraint.

The case $l = 2$ is analyzed, considering two forces $f_1$ and $f_2$, whose intensities are random variables. Eq. (10) reads:

$$u_{i,1}^{unit} \bar{f}_1 + u_{i,2}^{unit} \bar{f}_2 + \boldsymbol{\Phi}^{-1}(1-P_{fail}) \times \left(\sigma_1^2 (u_{i,1}^{unit})^2 + \sigma_2^2 (u_{i,2}^{unit})^2 + 2\sigma_{12} u_{i,1}^{unit} u_{i,2}^{unit}\right)^{1/2} - u_{lim,i} \le 0. \tag{11}$$

Whit respect to the case of deterministic forces, the probabilistic setting calls for the additional term scaled by $\boldsymbol{\Phi}^{-1}(q)$, i.e the constraint becomes stricter. The term in brackets depends on the variances, $\sigma_1^2$ and $\sigma_2^2$, and the covariance, $\sigma_{12}$, of the intensity of the two considered forces.

Eq. (5d) prescribes a minimum value for the weight fraction of the porous microstructure, namely $w_f$. A lower bound $\rho_{g,min}$ applies due to manufacturing constraints. An upper bound $\rho_{g,max}$ is prescribed, as well. Both bounds are enforced in Eq. (5) through the statement of side constraints for the variables $\rho_{g,e}$.

### 2.3. Numerical implementation

Details are given in Section 2.3.1 on the treatment of the density fields to avoid numerical instabilities and control mesh-dependence. The well-known gradient-based Method of Moving Asymptotes (MMA) [48] is used to handle the multi-phase and multi-constrained optimization problem. The sensitivity of the probabilistic displacement constraints is computed as detailed in Section 2.3.2.

#### 2.3.1. Filtering

A standard linear filter [59,60] is implemented on all the element variables to avoid potential issues that are well-known in topology optimization, i.e. the arising of mesh dependence and checkerboard patterns. The original variables $\rho_{1,e}$, $\rho_{2,e}$, $\rho_{g,e}$ are mapped to the new sets $\tilde{\rho}_{1,e}$, $\tilde{\rho}_{2,e}$ and $\tilde{\rho}_{g,e}$ as follows:

$$\tilde{\rho}_{1,e} = \frac{1}{\sum_n H_{1,es}} \sum_n H_{1,es}\,\rho_{1,e}, \quad \tilde{\rho}_{2,e} = \frac{1}{\sum_n H_{2,es}} \sum_n H_{2,es}\,\rho_{2,e}, \quad \tilde{\rho}_{g,e} = \frac{1}{\sum_n H_{g,es}} \sum_n H_{g,es}\,\rho_{g,e} \tag{12a}$$

$$H_{1,es} = \max(0, r_{1,f} - d_{e,s}), \quad H_{2,es} = \max(0, r_{2,f} - d_{e,s}), \quad H_{g,es} = \max(0, r_{g,f} - d_{e,s}) \tag{12b}$$

where $d_{e,s}$ is the distance between the centroid of the $e$th and $s$th element, whereas $r_{1,f}$, $r_{2,f}$ and $r_{g,f}$ are the filter radius used for $\rho_{1,e}$, $\rho_{2,e}$ and $\rho_{g,e}$, respectively. The filters on $\rho_{1,e}$ and $\rho_{2,e}$ can be used to control heuristically the minimum size of the features arising in the optimal layout, for solid and porous material respectively. The filter

for $\rho_{g,e}$ can be used to promote a smooth variation of the density of the graded material throughout the region occupied by the porous phase.

The filtered densities $\tilde{\rho}_{1,e}$ and $\tilde{\rho}_{2,e}$ are mapped to the set of projected (physical) densities $\hat{\rho}_{1,e}$ and $\hat{\rho}_{2,e}$, respectively, in order to achieve $0-1$ solutions, i.e. a clear separation between full material and porous material or void. The formulation proposed in [61] is herein adopted:

$$\hat{\rho}_{1,e} = \frac{\tanh(\beta\eta) + \tanh(\beta(\tilde{\rho}_{1,e} - \eta))}{\tanh(\beta\eta) + \tanh(\beta(1-\eta))}, \quad \hat{\rho}_{2,e} = \frac{\tanh(\beta\eta) + \tanh(\beta(\tilde{\rho}_{2,e} - \eta))}{\tanh(\beta\eta) + \tanh(\beta(1-\eta))}, \tag{13}$$

with threshold $\eta = [0,1]$ and sharpness factor $\beta = [1,\infty]$ in both cases. The Heaviside function projects densities below the threshold to 0 and densities above it to 1, depending on the value of the sharpness factor, see e.g. [62,63]. In the numerical section $\eta = 0.5$, whereas $\beta$ is smoothly increased during the simulations from 2 to 16 by means of the continuation approach in [52].

### 2.3.2. Sensitivity computation

Sensitivity of the objective function and of the constraints are needed to run the gradient-based minimizer. The derivative of Eq. (10) with respect to the element unknown $\rho_k$, which can be indifferently an entry of $\boldsymbol{\rho_1}$, $\boldsymbol{\rho_2}$ or $\boldsymbol{\rho_g}$, may be computed as:

$$\sum_{j=1}^{l} \frac{\partial u_{i,j}^{unit}}{\partial \rho_k} \bar{f}_j + \Phi^{-1}(q)(\mathbf{u}_i^{unit})^T \mathbf{K}_{ov} \frac{\partial \mathbf{u}_i^{unit}}{\partial \rho_k} \left( (\mathbf{u}_i^{unit})^T \mathbf{K}_{ov} \mathbf{u}_i^{unit} \right)^{-1/2}, \tag{14}$$

The sensitivity of $u_{i,j}^{unit}$ may be computed through the adjoint method, see e.g. [2]. Accordingly, $u_{i,j}^{unit}$ in Eq. (6) does not change when adding at the right hand side a zero function derived from the equilibrium of Eq. (5b):

$$-\lambda_i^T \left( \mathbf{K}(\boldsymbol{\rho_1}, \boldsymbol{\rho_2}, \boldsymbol{\rho_g}) \mathbf{U}_j^{unit} - \mathbf{F}_j^{unit} \right), \tag{15}$$

where $\lambda_i$ is any arbitrary but fixed vector and it is assumed that $\mathbf{F}_j$ does not depend on $\boldsymbol{\rho_1}, \boldsymbol{\rho_2}, \boldsymbol{\rho_g}$. After re-arrangement of terms, the derivative of $u_{i,j}^{unit}$ with respect to the element unknown $\rho_k$ reads:

$$\frac{\partial u_{i,j}^{unit}}{\partial \rho_k} = \left( \boldsymbol{L}_i^T - \lambda_i^T \mathbf{K}(\boldsymbol{\rho_1}, \boldsymbol{\rho_2}, \boldsymbol{\rho_g}) \right) \frac{\partial \mathbf{U}_j^{unit}}{\partial \rho_k} - \lambda_i^T \frac{\partial \mathbf{K}(\boldsymbol{\rho_1}, \boldsymbol{\rho_2}, \boldsymbol{\rho_g})}{\partial \rho_k} \mathbf{U}_j^{unit}, \tag{16}$$

that can be in turn written as:

$$\frac{\partial u_{i,j}^{unit}}{\partial \rho_k} = -\lambda_i^T \frac{\partial \mathbf{K}(\boldsymbol{\rho_1}, \boldsymbol{\rho_2}, \boldsymbol{\rho_g})}{\partial \rho_k} \mathbf{U}_j^{unit}, \tag{17}$$

where $\lambda_i$ satisfies the adjoint equation:

$$\mathbf{K}(\boldsymbol{\rho_1}, \boldsymbol{\rho_2}, \boldsymbol{\rho_g}) \lambda_i = \left( \frac{\partial u_{i,j}^{unit}}{\partial \mathbf{U}_j^{unit}} \right)^T = \mathbf{L}_i. \tag{18}$$

The derivatives in Eq. (17) can be evaluated accounting for the material law in Eq. (1). The sensitivity of the objective function and the weight constraint in Eq. (5c) are straightforward. The derivatives with respect to the filtered variables ($\tilde{\rho}_{1,e}$, $\tilde{\rho}_{2,e}$. $\tilde{\rho}_{g,e}$) and the projected ones ($\hat{\rho}_{1,e}$, $\hat{\rho}_{2,e}$) can be easily evaluated by applying the chain rule to Eqs. (12) and Eqs. (13), respectively. It is also remarked that, at each iteration, only one inverse of the stiffness matrix $\mathbf{K}(\boldsymbol{\rho_1}, \boldsymbol{\rho_2}, \boldsymbol{\rho_g})$ must be computed to evaluate constraints and their sensitivities. Indeed the linear systems in Eqs. (5) and (18) share the same coefficient matrix. The overall process is repeated until convergence is achieved, i.e. the maximum difference in terms of the values of the set of minimization unknowns $\rho_{1,e}$, $\rho_{2,e}$ and $\rho_{g,e}$ between two subsequent steps is less than $10^{-3}$.

## 3. Numerical studies

Four numerical examples are presented to assess the method introduced in Section 2. The constraints enforced to govern the deflection are such that, in each one of the considered nodes, the controlled component of the displacement is not allowed to exceed $\alpha$ times that computed adopting $\rho_1 = 1$ everywhere (full material in the entire design domain). In Example 1 it is assumed that $\alpha = 3.0$, whereas $\alpha = 1.5$ is used for Example 2 and Example 4. The assumption $\alpha = 2.5$ is done in Example 3. Geometry and boundary conditions are those presented in Fig. 3. If not differently specified, the filter radii used in the simulations are $r_{1,f} = r_{2,f} = L/10$, for $\rho_{1,e}$ and $\rho_{2,e}$, whereas $r_{g,f} = 3 \times L/10$ is adopted for $\rho_{g,e}$. Solutions are generated by enforcing different values of $w_f \geq 0$ in the formulation of Eq. (5). For each numerical investigation, the weight of the achieved optimal design is given in terms of the ratio $W/W_0$, where $W$ is the weight at convergence and $W_0$ is the weight of the entire design domain made of full material. All the presented layouts fulfill the enforced displacement constraints. The accepted probability failure is $P_{fail} = 0.1$, if not differently specified.

The adoption of self-supporting infills relieves manufacturing issues when fabricating the achieved optimal layouts with 3d-printing techniques. However, there are many sources of uncertainties related to additive manufacturing. Among the others, the work in [64] analyzes the main factors that govern defect sensitivity in additive manufacturing, with special regard to the fabrication of architected porous microstructures. Macroscopic mechanical properties are sensitive to intrinsic characteristics of the base material, defects affecting geometrical features of the printed microstructure, process parameters, pre- and post-process treatments, to mention a few. A workflow is suggested to handle these issues, starting from the fabrication of prototypes, exploiting nondestructive techniques for defect detection and uncertainty quantification for an estimate of the impact of defects, see also [65], to end up with the formulation of problems of robust topology optimization. The investigation presented in this contribution is limited to probabilistic loading, mainly focusing on the impact of this type of uncertainty on the shape of the optimal layouts and the load paths they provide. The implementation of the workflow presented in [64] would remarkably improve robustness of the achieved results.

The simulations herein considered refer to two-dimensional examples only. It is remarked that the method presented in Section 2 holds both in two and three dimensions, provided that suitable porous microstructures are used especially considering overhang issues, see [66]. Moving from a pixel-based optimization, in 2D, to a voxel-based one, in 3D, implies a remarkable increase in terms of computational time. The bottle neck of the procedure resides in the finite element analysis required at each step of the optimization to compute the current value of the constraints and their sensitivity. Parallel computing can be conveniently adopted to address medium and large scale three-dimensional examples. Reference is made in particular to the work in [67], providing a flexible framework for parallel topology optimization, including a parallel implementation of the gradient-based minimizer MMA.

### 3.1. Cantilever beam

A preliminary assessment of the numerical implementation is given addressing the cantilever beam sketched in Fig. 3(a). Filter radii $r_{1,f} = r_{2,f} = L/30$ and $r_{g,f} = L/10$ are assumed in this investigation. When a single force acts upon the structure, the work of the external load at equilibrium is equal to the scalar product of the force itself and the displacement at the loaded point along the direction of the force. In this case, minimizing the compliance under a volume constraint is equivalent (up to a scaling) to minimizing the weight while controlling the displacement component that is involved in the definition of the work, see [68].

A deterministic problem of volume-constrained minimum compliance for the cantilever represented in Fig. 3(a) has been tackled, among the others, in [5] and [69]. The result found using the displacement-constrained formulation of Eq. (5), assuming deterministic load $f_1$, $\alpha = 3.0$, $w_f = 0$, and $0.05 \leq \rho_g \leq 0.65$, is shown in Fig. 4. The achieved layout is independent on the type of infill selected in the material interpolation law of Eq. (1). The weight at convergence is $W/W_0 = 0.252$. The optimal topology is in good agreement with those

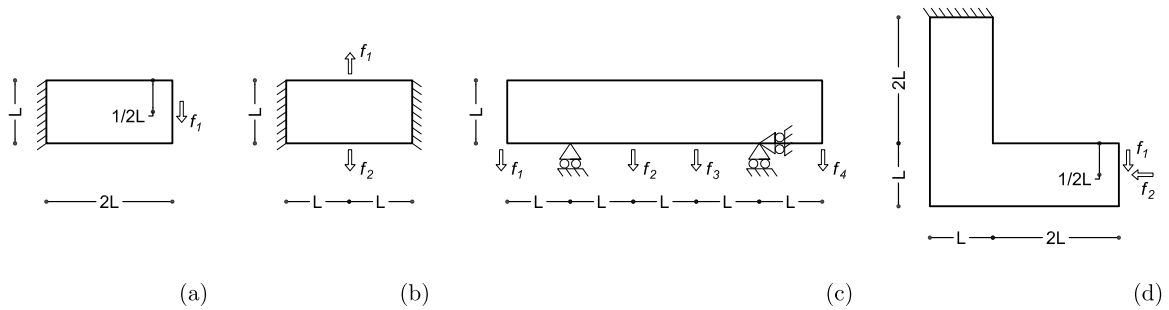


**Fig. 3.** Geometry and boundary conditions for the numerical examples.

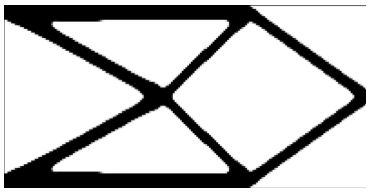

**Fig. 4.** Example 1. Optimal design in case of a deterministic force $f_1$, $W/W_0 = 0.252$.

found in [69] when investigating minimum compliance design for low volume fraction and small filter radius, both working with SIMP and using an interpolation scheme based on the Hashin–Strikhman upper bounds for bulk and shear moduli. As discussed in [3], the power-law interpolation introduced in [1] may be also regarded as a material law, meaning that a microstructure of solid and void can be found to match the elastic properties at intermediate densities, with a power $p \geq 3$.

The displacement-constrained formulation of Eq. (5) is then tested for probabilistic loading, assuming unitary average value $\bar{f}_1$ and coefficient of variation $CV_1 = 0.15$. Denoting by $u_1$ the vertical displacement at the point loaded by $\bar{f}_1$, the deterministic inequality that is equivalent to the probabilistic displacement constraint simplifies to:

$$c_1 u_1 \leq u_{lim}, \text{ with } c_1 = 1 + \Phi^{-1}(1 - P_{fail})\sigma_1,$$

see Eqs. (10) and (11). This is in turn equivalent to solving a deterministic problem in which the controlled displacement cannot exceed $1/c_1 \cdot 3.0 = 2.52$ times that computed adopting $\rho_1 = 1$ everywhere. The allowed displacement $1/c_1 \cdot u_{lim}$ is nearly 16% less than the limit prescribed in the problem involving deterministic loading ($u_{lim}$). The optimal design found for $w_f = 0$ in case of probabilistic loading is represented in Fig. 5(a). Again, the solution is independent on the type of infill selected in the material interpolation law. The achieved layout is similar to that shown in Fig. 4, with an increase in terms of weight that is around 16%, as expected.

In Fig. 5(b), the optimal design using an infill of diamond lattice is shown, as found enforcing $w_f = 0.125$ in the formulation of Eq. (5). A composite structure arises that is made of an inner gray area, standing for low density infill, surrounded by a layer of solid material. The weight is nearly 6% larger than in the previous case. A similar layout was retrieved in [5] when investigating minimum compliance design using an interpolation scheme derived from the homogenization of a diamond lattice. The composite layout was shown to be a sub-optimal solution with respect to the design made of full material and void only. Indeed, the optimal solution was found using rank-2 laminates having orthogonal layers aligned with the principal stresses, see in particular [70]. This was expected, since the optimal set of elasticity tensors for rank-2 material is defined without any restriction related to the adoption of cells having given orientation.

A final investigation on the cantilever of Example 1 is performed using the code provided in [5] for volume-constrained minimum compliance with rank-2 material. The input volume is iteratively changed to match a final value of the structural compliance corresponding to $\alpha = 1/c_1 \cdot 3.0 = 2.52$. The relevant distribution of rank-2 material is that represented in Fig. 6. The weight is $W/W_0 = 0.268$, approximately 12% lighter than the design made of full material and void in Fig. 5(a), and almost 19% lighter than the composite solution in Fig. 5(b). This is in agreement with the findings reported above.

In the next sections, rank-2 laminates will be disregarded to focus on restricted design problems in which solid material is distributed along with graded microstructures of the type in Fig. 1. According to [5], this may be seen as a parameterized unit cell design based on density, which provides far less flexibility than any approach involving a local optimization problem.

The effect of multiple forces will be considered. At first, optimal solutions made of solid and void will be investigated for $w_f = 0$. Then, the enforcement $w_f > 0$ will be exploited to address the design of composite elements. The adoption of an infill with given layout and orientation is sub-optimal in terms of structural performance, but can be beneficial especially to prevent manufacturing issues.

### 3.2. Short beam with fixed ends

A further assessment of the formulation considering uncertainties in the loading amplitude is given through elaborations on Example 2, see the short beam with fixed ends shown in Fig. 3(b). The setting $w_f = 0$ is used throughout this investigation, meaning that no porous phase is required. Assuming that two forces with deterministic amplitude $f_1 = f_2$ are applied at midspan at the top and at the bottom of the specimen, respectively, the optimal 0-1 design is that shown in Fig. 7. It consists of a straight tie whose cross-section provides the required stiffness. The weight at convergence of this self-equilibrated solution is $W/W_0 = 0.079$.

Probabilistic loading is subsequently addressed, assuming that the average value for both point forces is unitary.

At first, the case of uncorrelated forces with coefficient of variations $CV_1 = CV_2 = 0.05$ is considered. The solutions found for two different values of the accepted failure probability of the displacement constraints are shown in Fig. 8. A heavier completely constrained statically determinate structure arises that can handle scenarios in which the upper and the lower forces are not equal in magnitude. To this goal, the middle vertical bar is connected to the ground by means of inclined elements converging to the corners of the design domain. Accepting a $P_{fail} = 0.01$, instead of $P_{fail} = 0.1$, does not affect the layout of the solutions, but requires a weight increase of around 25%. The setting $P_{fail} = 0.1$ will be used throughout the numerical section.

Additional investigations are performed with respect to the case of uncorrelated forces, considering different assumptions for the coefficient of variations of the magnitude of the two forces. Assuming that $CV_1 = CV_2 = 0.15$, the design represented in Fig. 9 is achieved. The increased standard deviation calls for an heavier design with respect to that shown in Fig. 8(a), with thicker members and no inner cavity. Assuming that $CV_1 = 0.15$ and $CV_2 = 0.05$, the symmetry of the optimal solution is broken, see Fig. 9(b). Only the inclined members

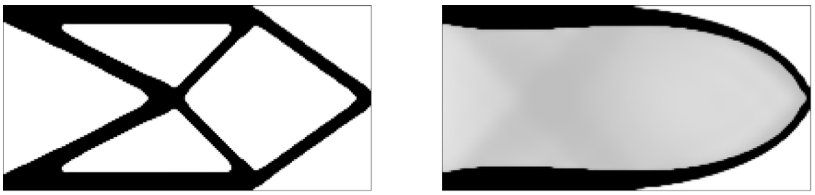

(a) (b)

**Fig. 5.** Example 1. Optimal design in case of a force $f_1$ with $CV_1 = 0.15$ prescribing: $w_f = 0$, $W/W_0 = 0.300$ (a); $w_f = 0.125$ with an infill of diamond lattice (D), $W/W_0 = 0.318$ (b).

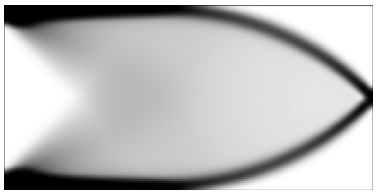

**Fig. 6.** Example 1. Optimal design using the code in [5] for rank-2 material, achieving $\alpha = 2.52$, $W/W_0 = 0.268$.

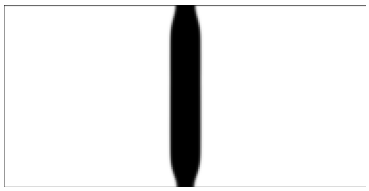

**Fig. 7.** Example 2. Optimal design in case of deterministic forces, $W/W_0 = 0.079$.

connecting the load with higher variability to the ground survive in the optimal solution. As expected the relevant weight ratio is in between that of the layout found for $CV_1 = CV_2 = 0.05$ and that of the case $CV_1 = CV_2 = 0.15$.

The effect of correlation is further explored considering two additional scenarios, i.e. perfectly positive correlation and perfectly negative correlation. When $r_{12} = 1$ any change in value of $f_1$ is exactly proportional to the change in value of $f_2$, occurring in the same direction. The relevant optimal design, which is represented in Fig. 10(a) ($W/W_0 = 0.088$), has the same layout of the self-balanced solution depicted in Fig. 7. With respect to the deterministic solution, the increase in weight is needed to account for the (perfectly correlated) variability of the amplitude of the two forces. When $r_{12} = -1$, the change in value of $f_1$ and $f_2$ are exactly proportional, but an increase in $f_1$ means a decrease in $f_2$ and viceversa. The optimal layout found for perfectly negative correlation is that given in Fig. 10(b). This resembles the layout found in case of uncorrelated load, see Fig. 8(a), but requires an increase in weight of around 12%.

### 3.3. Simply-supported beam

Example 3 addresses the simply-supported beam with overhangs represented in Fig. 3(c). Four point forces are symmetrically applied at the lower edge of the rectangular design domain. The optimal design found for $w_f = 0$ when considering the amplitude of the forces as deterministic and equal in value is represented in Fig. 11. Two independent structures arise around the supports, whose rotational equilibrium requires $f_1 = f_2$ and $f_3 = f_4$. No porous phase is found.

Assuming that the forces are uncorrelated, all with the same average value and coefficient of variation equal to 0.25, a completely constrained statically determinate structure arises, see Fig. 12. The weight at convergence of this 0-1 solution is $W/W_0 = 0.497$, with an increase not far from 60% with respect to the layout found in case of deterministic loads.

When looking at correlated forces, four cases are considered, which are:

case $A$: $r_{12} = r_{23} = r_{34} = 0.5,\ r_{13} = r_{24} = -0.5,\ r_{14} = -1,$
case $B$: $r_{12} = r_{13} = r_{14} = r_{23} = r_{24} = r_{31} = -0.33,$
case $C$: $r_{12} = r_{13} = r_{24} = r_{34} = -1,\ r_{14} = r_{23} = 1,$
case $D$: $r_{12} = r_{14} = r_{23} = r_{34} = -1,\ r_{13} = r_{24} = 1.$

The achieved optimal layouts are reported in Fig. 13. In case $A$, the correlation of any force is positive with forces whose application point is not farther than $L$, otherwise negative. It is recalled that, for positive correlation two variables tend to change in the same direction, whereas negative correlation describes variables that tend to move in opposite direction from one another. The relevant design, see Fig. 13(a), is lighter than that found in case of uncorrelated loads, exhibiting a slightly different design only in the central region. In case $B$, addressing negative correlation for all the forces, the optimal layout, see Fig. 13(b), has the same topology of that represented in Fig. 12, with a minor increase in terms of weight. Case $C$ addresses perfectly positive correlation between the forces applied at the tip of the overhangs and between those applied in the central span, whereas perfectly negative correlation is prescribed between forces of the former and the latter group. The relevant optimal design is that represented in Fig. 13(c). In the central region of the specimen only horizontal bars arise, since no shear is expected. However, the overall weight is 10% larger than for uncorrelated forces, due to the increased bending moments the specimen is likely to undergo. In case $D$, perfectly positive correlation is assumed between $f_1$ and $f_3$, and between $f_2$ and $f_4$, whereas perfectly negative correlation for the remaining combinations. The relevant optimal design, which is represented in Fig. 13(d), is characterized by a cross-shaped layout in the central region that provides bracing according to the expected shear internal action. In this case, the optimal layout is much lighter (nearly 20%) than that found when no correlation is assumed among the forces.

Further numerical investigations are performed, focusing on uncorrelated forces and enforcing a minimum weight of the porous phase. The setting $w_f = 0.25$ is used in the simulations that follow. At first, it is assumed that the density of the porous material can range between 0.25 and 0.65, due for instance to manufacturing constraints. The optimal layouts are represented in Fig. 14, considering the three infills introduced in Section 2.1, plotting maps of the overall density $\rho_{1,e} + (1 - \rho_{1,e})\rho_{2,e}\rho_{g,e}$. Black regions stand for full material, i.e. $\rho_{1,e} = 1$, whereas gray scale gives information on the density of the porous phase $0.25 \leq \rho_{g,e} \leq 0.65$. Indeed, where a porous phase arises, $\rho_{1,e} = 0$ and $\rho_{2,e} = 1$, meaning that the overall density correspond with $\rho_{g,e}$, see Section 2.1. When using an isotropic microstructure consisting of an HCP arrangement of graded circular holes, the optimal design is that represented in Fig. 14(a). It consists of a coated structure, in which solid material encloses an inner region of infill whose density is not homogeneously distributed. In Fig. 14(b), the optimal layout found when adopting the orthotropic diamond infill is represented. Solid

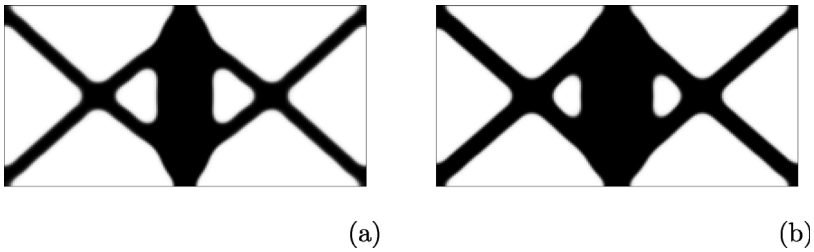


**Fig. 8.** Example 2. Optimal design in case of uncorrelated forces for different values of the accepted failure probability ($CV_1 = CV_2 = 0.05$) : $P_{fail} = 0.1$, $W/W_0 = 0.305$ (a); $P_{fail} = 0.01$, $W/W_0 = 0.384$ (b).

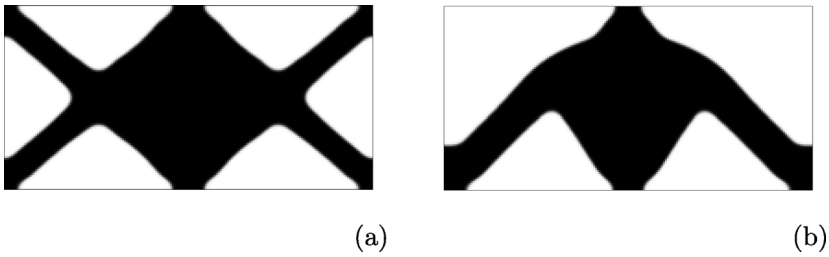


**Fig. 9.** Example 2. Optimal design in case of uncorrelated forces for different values of the coefficient of variation ($P_{fail} = 0.1$): $CV_1 = CV_2 = 0.15$, $W/W_0 = 0.516$ (a); $CV_1 = 0.15$, $CV_2 = 0.05$, $W/W_0 = 0.440$ (b).

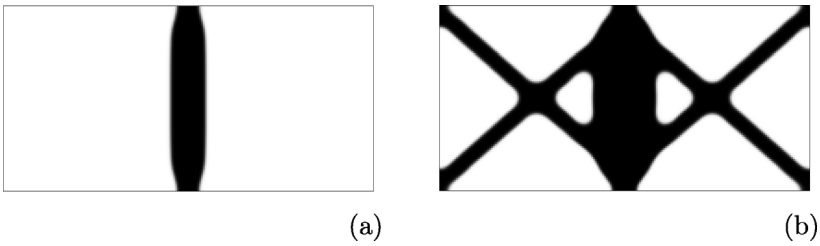


**Fig. 10.** Example 2. Optimal design in case of correlated forces for different values of the correlation ($CV_1 = CV_2 = 0.05$, $P_{fail} = 0.1$): $r_{12} = 1$, $W/W_0 = 0.088$ (a); $r_{12} = -1$, $W/W_0 = 0.342$ (b).

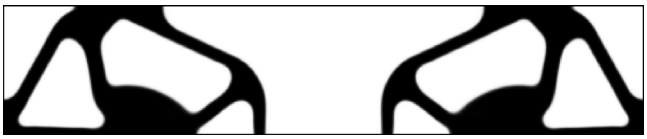

**Fig. 11.** Example 3. Optimal design in case of deterministic forces, $W/W_0 = 0.315$.

**Fig. 12.** Example 3. Optimal design in case of uncorrelated forces ($CV = 0.25$ for all forces, $P_{fail} = 0.1$), $W/W_0 = 0.497$.

material is used to build the upper and the lower chord, in addition to vertical elements that divide the layout in square bays. Some of them are completely filled with the porous phase, whereas some others are braced by inclined members oriented along the direction of maximum stiffness of the infill, i.e. ±45° with respect to the vertical axis, see Fig. 2. The optimal layout found in conjunction with the orthotropic elongated diamond infill is presented in Fig. 14(c). The upper and lower chord of solid material still exist, but bracing is given by elements of porous material inclined of ±30° with respect to the vertical axis, i.e. along the direction of maximum stiffness for the adopted porous structures, see again Fig. 2. Some connections with the lower chord are made in full material.

The enforcement of $w_f > 0$ comes with an increase in terms of the final weight with respect to the solution given in Fig. 12 that reads 9%, 7% and 6% for the hexagonal close-packing of circular holes, the diamond lattice, and the elongated diamond lattice, respectively.

The material law in Eq. (1) allows for a direct control of the minimum and maximum density of the porous phase that arise in the optimal design. Indeed this is implemented by means of side constraints in Eq. (5). A further set of simulations is performed for $w_f = 0.25$, assuming that the density of the porous material can range between 0.25 and 0.45. The achieved optimal layouts are presented in Fig. 15. For all of them the increase in terms of weight is negligible with respect to the relevant composite structures given in Fig. 14. The layout found for the hexagonal close-packing of circular holes is made of a solid coating, which is almost entirely filled by a region of porous material with homogeneous density, see Fig. 15(a). The reduction in the maximum density of the infill calls for the adoption of solid elements crossing the porous phase to connect the chords and provide the requested stiffness to fulfill displacement constraints. Concerning the orthotropic infills, in the optimal layout of Fig. 15(b) almost all the squared bays originally observed in Fig. 14(b) are completely filled with porous material. The solution presented in Fig. 15(c) preserves the same layout of the axes of the bracing elements already commented on when addressing Fig. 15(c), whereas the geometry of the solid elements connecting the lower chord to the inclined bar is affected by major modifications.

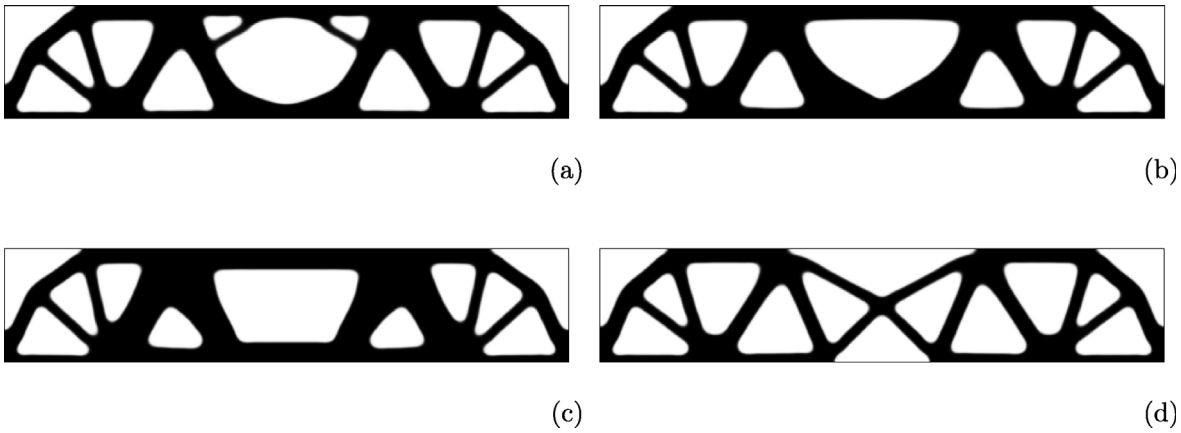


**Fig. 13.** Example 3. Optimal design in case of correlated forces for different values of the correlation ($CV = 0.25$ for all forces, $P_{fail} = 0.1$): case $A$, $W/W_0 = 0.478$ (a); case $B$, $W/W_0 = 0.514$ (b); case $C$, $W/W_0 = 0.551$ (c); case $D$, $W/W_0 = 0.407$ (d).

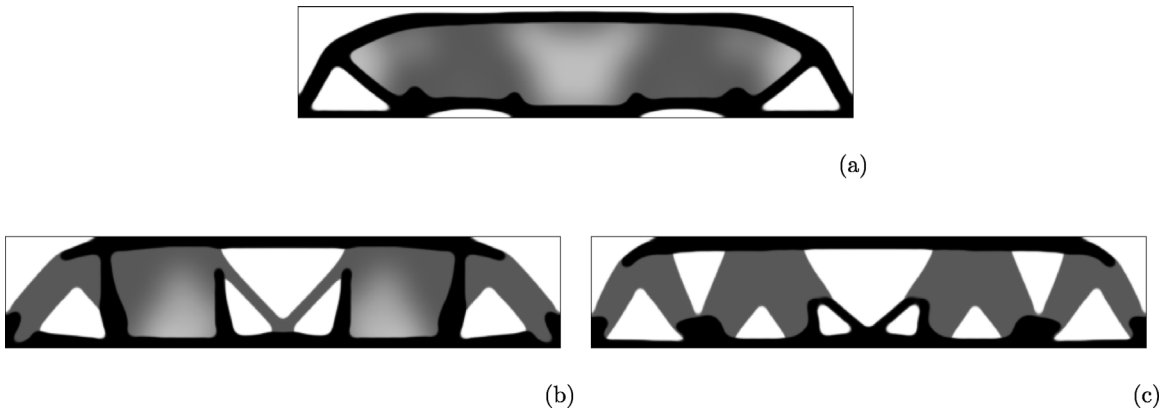


**Fig. 14.** Example 3. Optimal design in case of uncorrelated forces ($CV = 0.25$ for all forces, $P_{fail} = 0.1$) enforcing $w_f = 0.25$ and $0.25 \leq \rho_g \leq 0.65$, using an infill of: hexagonal close-packing of circular holes (HCP), $W/W_0 = 0.542$ (a); diamond lattice (D), $W/W_0 = 0.532$ (b); elongated diamond lattice (E), $W/W_0 = 0.526$ (c).

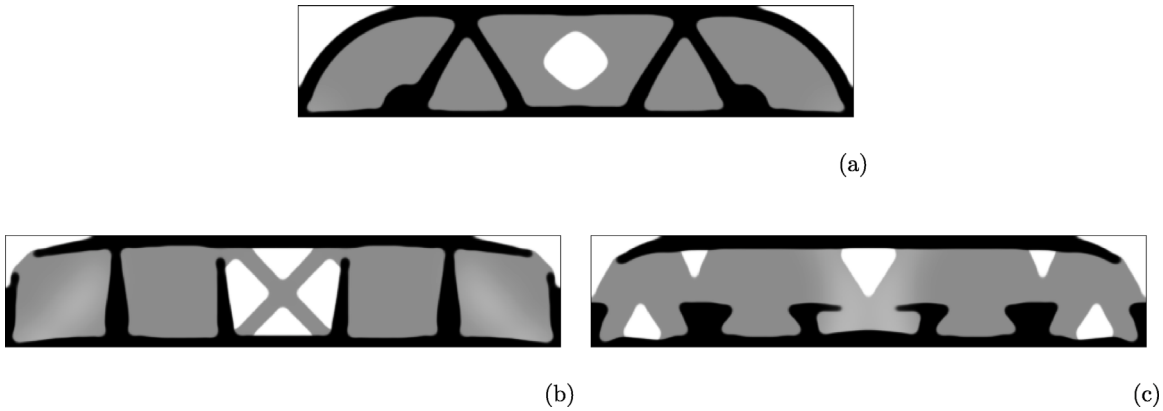


**Fig. 15.** Example 3. Optimal design in case of uncorrelated forces ($CV = 0.25$ for all forces, $P_{fail} = 0.1$) enforcing $w_f = 0.25$ and $0.25 \leq \rho_g \leq 0.45$, using an infill of: hexagonal close-packing of circular holes (HCP), $W/W_0 = 0.560$ (a); diamond lattice (D), $W/W_0 = 0.529$ (b); elongated diamond lattice (E), $W/W_0 = 0.547$ (c).

Notwithstanding the (moderate) increase in terms of weight, the adoption of composite solutions may provide peculiar advantage over a 0-1 layout, including redundancy of load pathes and high bending stiffness-to-weight ratio. In particular, the adoption of a support-free infill can solve overhang issues when manufacturing blueprints of the layout achieved through optimization via layer-by-layer 3d-printing. In the optimal solution given in Fig. 12 several elements of the upper chords call for ad hoc supports, since their orientation with respect to the vertical axis is not compatible with the admissible overhang angle, typically $\pm 45°$. In the layouts presented in Fig. 15, the need of additional supports is remarkably reduced and only few limited portions of the upper chord remain unsupported by the infill, see in particular Fig. 15(b) and (c). To avoid the arising of any unsupported region, one may leverage on the material law in Eq. (1) by specifying "passive" domains for the variable $\rho_{2,e}$, see e.g. [2]. Indeed, by setting $\rho_{2,e} = 1$ in a certain domain, either a solid phase or an infill region may arise there. In Fig. 16 optimal layouts found prescribing passive domains in the region between the upper and lower chord are presented. Minor modifications affect the topology of the solid material, when compared to the layouts of Fig. 15. The increase in weight to achieve

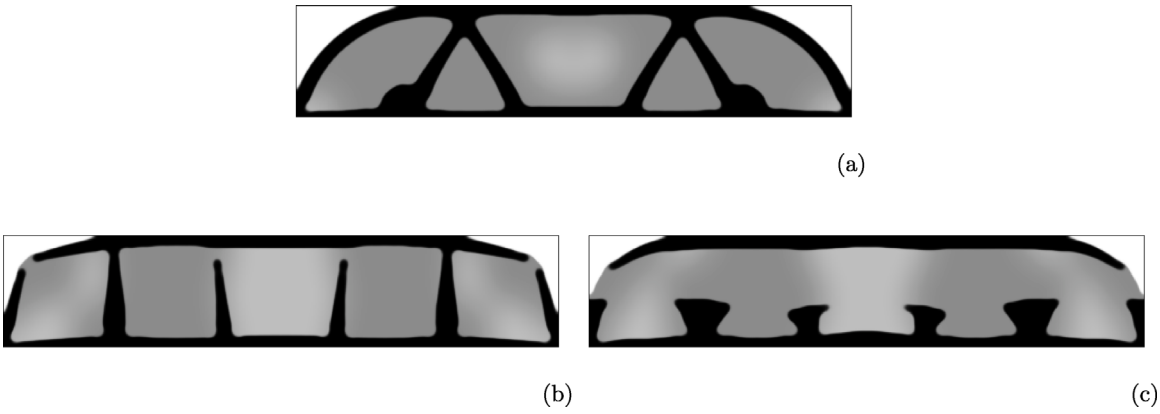


**Fig. 16.** Example 3. Optimal design in case of uncorrelated forces ($CV = 0.25$ for all forces, $P_{fail} = 0.1$) enforcing $w_f = 0.25$ and $0.25 \le \rho_g \le 0.45$, using passive regions for $\rho_{2,e}$ and an infill of: hexagonal close-packing of circular holes (HCP), $W/W_0 = 0.563$ (a); diamond lattice (D), $W/W_0 = 0.530$ (b); elongated diamond lattice (E), $W/W_0 = 0.549$ (c).

**Table 2**
Example 3. $P_{fail}$ computed for the optimal layouts represented in Figs. 12 and 16, considering different cases of correlation of the forces.

| | Case *A* | Case *B* | Case *C* | Case *D* |
|---|---|---|---|---|
| 0-1 design, Fig. 12 | 0.078 | 0.128 | 0.214 | 0.140 |
| HCP-based design, Fig. 16(a) | 0.100 | 0.125 | 0.240 | 0.101 |
| D-based design, Fig. 16(b) | 0.107 | 0.126 | 0.247 | 0.079 |
| E-based design, Fig. 16(c) | 0.108 | 0.125 | 0.245 | 0.087 |

this print-ready layouts is negligible with respect to the previous set of solutions.

The optimal layouts represented in Figs. 12 and 16 are further investigated addressing their structural response in case of correlated loads. In Table 2, maximum values of the probability of failure for the considered displacement constraints are reported, addressing the four different cases already introduced. These have been computed by entering the displacements given by Eq. (5b) for different sets of density variables, and solving Eq. (10) for $P_{fail}$. The 0-1 layout achieved in case of uncorrelated forces exceeds the reference value (0.01) by a certain amount in the cases *B*, *C*, and *D*. For composite beams this happens only in the cases *B* and *C*, thus confirming the effective structural contribution provided by the graded porous phase when dealing with the shear-dominated case *D*.

### 3.4. L-shaped cantilever beam

Example 4 is concerned with the L-shaped cantilever shown in Fig. 3(d). The specimen is fully clamped along the top edge and is subjected to a vertical force with amplitude $f_1$, and a horizontal one with amplitude $f_2$. Both are applied at the middle point of the right edge of the domain. The optimal design found for $w_f = 0$, when considering the amplitude of the two forces as deterministic and equal in value, is represented in Fig. 17. The direction of the bar receiving the load is that of the resultant of the two forces. No other load combination can be effectively handled by such a layout. The weight at convergence is $W/W_0 = 0.479$.

Concerning probabilistic loading, two scenarios are dealt with in the numerical simulations that follow. In both cases, forces with the same average amplitude and equal coefficient of variation $CV = 0.25$ are considered. In Fig. 18(a), the optimal layout found in case of uncorrelated load is depicted, whereas Fig. 18(b) addresses forces with perfectly negative correlation. The former solution is heavier than the latter. The increase in weight with respect to the layout found for deterministic load is approximately 35% and 20%, respectively. Both layouts consist of a branched horizontal "beam" and a stiff corner region, but the "column" is lighter when using $r_{12} = -1$. Indeed, the

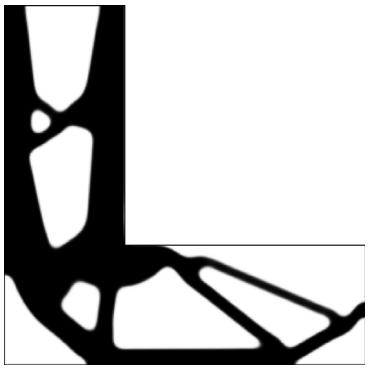

**Fig. 17.** Example 4. Optimal design in case of deterministic forces, $W/W_0 = 0.479$.

case of uncorrelated loading is expected to maximize the actions across the structure.

For the same probabilistic loads, optimal layouts are investigated enforcing $w_f = 0.125$ and using porous phases with density in the range $0.25 \le \rho_g \le 0.45$.

At first, the case of uncorrelated loads is considered, see Fig. 19. Independently of the type of lattice that is used to design the porous phase, (i) the corner region is made of full material and, (ii) both in the beam and in the column, some solid elements fully or partially enclose a region of infill whose density is smoothly distributed. No additional bracing crosses the porous zones. It may be also noticed that the interface between any orthotropic infill and void is parallel to the direction of maximum stiffness of the porous material. Adopting the considered layouts, no additional support is needed within the chords to build the specimens. This comes with a weight increase with respect to the solution given in Fig. 18(a) equal to 4%, 1% and 2% for the hexagonal close-packing of circular holes, the diamond lattice, and the elongated diamond lattice, respectively. Although the optimal layouts represented in Fig. 19 share a similar overall topology, minor differences remarkably affect the mechanical response of the specimens. A cross-check is performed evaluating the maximum value of $P_{fail}$ when each one of the optimal material distributions represented in Fig. 19 is used in conjunction with the elastic properties of the other porous microstructures. Variations in the range $10\% - 200\%$ are reported, see Table 3. It must be also remarked that convergence to a global minimum cannot be guaranteed for the herein addressed non-convex problem, see in particular [2] and [4]. In each row of the table, $P_{fail}$ is minimum (and equal to 0.01) when the analysis is performed considering the material for which the layout has been designed. This confirms that, among the analyzed solutions, no better local minima exists.

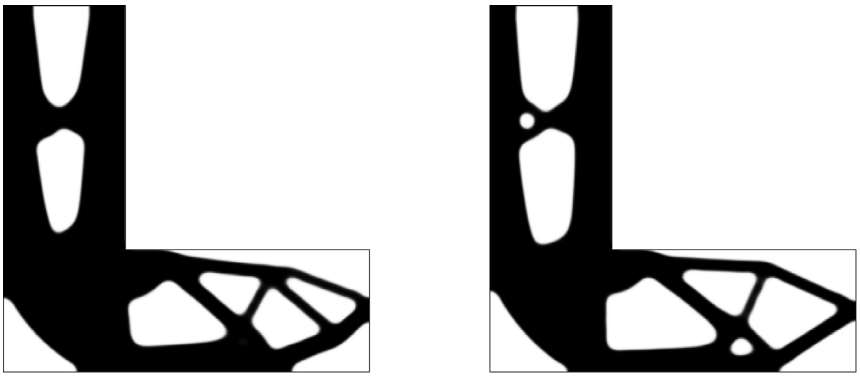


**Fig. 18.** Example 4. Optimal design in case of forces ($CV = 0.25$ for all forces, $P_{fail} = 0.1$) which are: uncorrelated, $W/W_0 = 0.641$ (a); correlated with $r_{12} = -1$, $W/W_0 = 0.572$ (b).

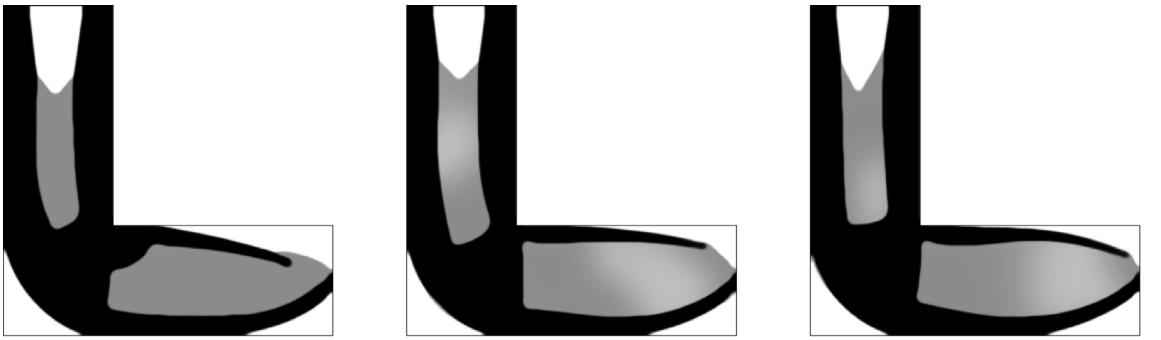


**Fig. 19.** Example 4. Optimal design in case of uncorrelated forces ($CV = 0.25$ for all forces, $P_{fail} = 0.1$) enforcing $w_f = 0.125$ and $0.25 \le \rho_g \le 0.45$, using an infill of: hexagonal close-packing of circular holes (HCP), $W/W_0 = 0.667$ (a); diamond lattice (D), $W/W_0 = 0.644$ (b); elongated diamond lattice (E), $W/W_0 = 0.652$ (c).

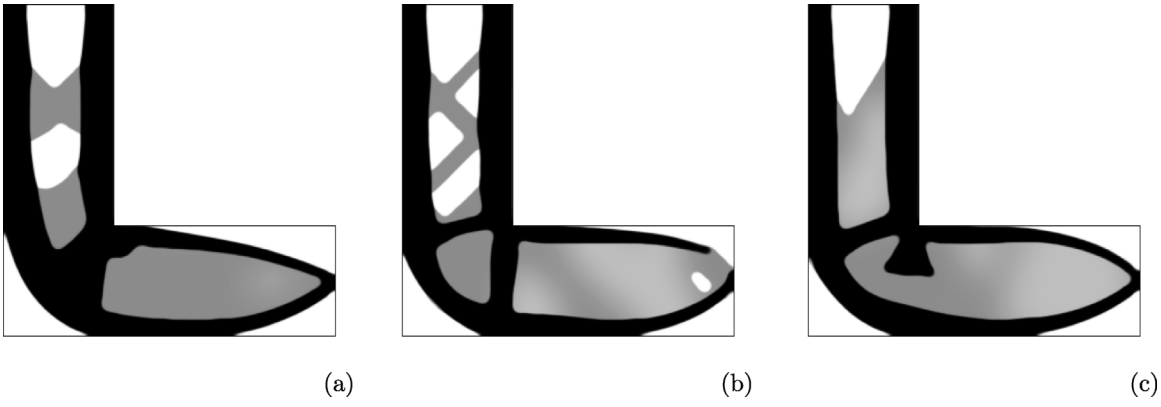


**Fig. 20.** Example 4. Optimal design in case of correlated forces with $r_{12} = -1$ ($CV = 0.25$ for all forces, $P_{fail} = 0.1$) enforcing $w_f = 0.125$ and $0.25 \le \rho_g \le 0.45$, using an infill of: hexagonal close-packing of circular holes (HCP), $W/W_0 = 0.597$ (a); diamond lattice (D), $W/W_0 = 0.574$ (b); elongated diamond lattice (E), $W/W_0 = 0.576$ (c).

A further set of simulations is performed accounting for the case in which perfectly negative correlation applies. The achieved optimal layouts are shown in Fig. 20. The enforcement of $w_f > 0$ comes with an increase in terms of the final weight with respect to the solution given in Fig. 18(b) that is around 4% for the hexagonal close-packing of circular holes and less than 1% for both the orthotropic lattices. The topology of the corner region is highly affected by the selected type of lattice. Full material is extensively used in the design when the hexagonal close-packing of circular holes is considered. A region of infill enclosed by solid members arises when using the diamond microstructures. A feature similar to that already seen along the lower chord of the composite design in Fig. 16(c) is retrieved in the optimal solution implementing the elongated diamond infill. While the optimal design in Fig. 20(c) has no cavity within the infill regions, the solutions depicted in Fig. 20(a) and (b) present some inner voids. To get rid of these features, passive regions could be introduced for $\rho_{2,e}$, as done in Example 3. Alternatively, the value of the filter radius for $\rho_{2,e}$ is herein increased to $r_{2,f} = 3 \times L/10$. The achieved layout are those represented in Fig. 21. As already found for the optimal solution in Fig. 20(c), no additional support is needed to manufacture the infill inside the coating. This modification has a negligible cost in terms of final weight.

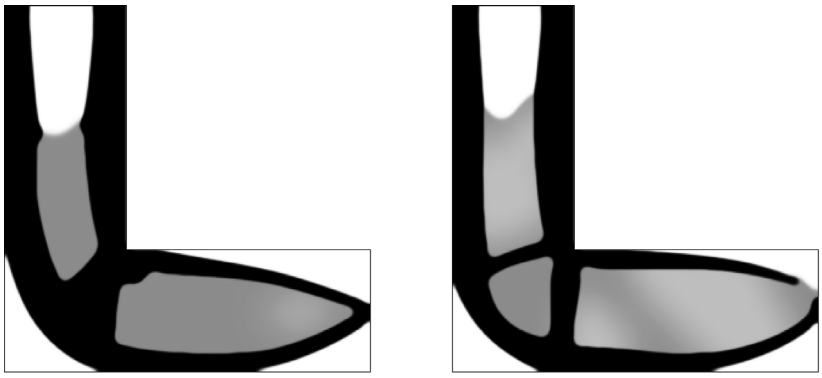


**Fig. 21.** Example 4. Optimal design in case of correlated forces with $r_{12} = -1$ ($CV = 0.25$ for all forces, $P_{fail} = 0.1$) enforcing $w_f = 0.125$ and $0.25 \le \rho_g \le 0.45$, using $r_{2,f} = 3 \times L/10$ and an infill of: hexagonal close-packing of circular holes (HCP), $W/W_0 = 0.601$ (a); diamond lattice (D), $W/W_0 = 0.575$ (b).

**Table 3**
Example 4. $P_{fail}$ computed for the optimal material distributions represented in Fig. 19, considering different porous microstructures.

| | Analysis performed with: | | |
|---|---|---|---|
| | HCP infill | D infill | E infill |
| HCP-based design, Fig. 19(a) | (0.100) | 0.112 | 0.121 |
| D-based design, Fig. 19(b) | 0.235 | (0.100) | 0.133 |
| E-based design, Fig. 19(c) | 0.166 | 0.107 | (0.100) |

**Table 4**
Example 4. $P_{fail}$ computed for the optimal material distributions represented in Figs. 20 and 21(c), considering different porous microstructures.

| | Analysis performed with: | | |
|---|---|---|---|
| | HCP infill | D infill | E infill |
| HCP-based design, Fig. 21(a) | (0.100) | 0.108 | 0.140 |
| D-based design, Fig. 21(b) | 0.968 | (0.100) | 0.420 |
| E-based design, Fig. 20(c) | 0.910 | 0.126 | (0.100) |

A final cross-check is operated comparing the mechanical response of the optimal layouts of Figs. 21 and 20(c), when adopting the elastic properties of different microstructures for the same optimal distribution of minimization unknowns. As expected, the outlined differences in terms of topology remarkably affect the computed values of the probability of failure for the considered displacement constraints, see Table 4.

## 4. Conclusions

A numerical method of homogenization-based topology optimization has been proposed, accounting for uncertainty in loading amplitude. Under the assumption of a joint normal distribution function to describe the uncertainty, stochastic displacement constraints can be re-written as a set of deterministic enforcements. This allows for the design of minimum weight structures for any accepted value of the probability to exceed a given displacement limit. A two-phase material law with void has been adopted to sketch composite structures made of a solid phase and a given fraction of graded infill with a prescribed layout. Numerical homogenization has been used to derive the macroscopic elastic constants of an isotropic and two orthotropic infills that are commonly used in additive manufacturing, i.e. an hexagonal arrangement of circular holes with high stiffness-to-weight ratio, and two self-supporting diamond lattices. Leveraging on the adopted material law, the admissible density range of the porous phase is effectively enforced by means of side constraints, whereas the optimization problem has been endowed with an additional enforcement to control the amount of graded infill to be distributed. Filtering procedures have been used to promote smooth variations in the spatial distribution of the infill and to control (heuristically) the size of the features arising in the optimal design. When combined with projection approaches, they have been used to achieve full separation of the phases. Sequential convex programming has been selected to solve the arising multi-constrained problem, resorting to the adjoint method for an efficient computation of the sensitivity.

Simulations have been performed to assess the proposed numerical method and to highlight peculiar features of the achieved optimal solutions in case of uncorrelated or correlated forces. When the constraint prescribing a minimum fraction of infill has been disregarded, the proposed formulation has retrieved 0-1 layouts characterized by a crisp solid-void interface. It has been shown that partially constrained layouts that may arise among statically determinate solutions in case of deterministic forces are generally replaced by completely constrained ones when uncertainties are accounted for. The cases of perfect correlation should be carefully regarded, see in particular Example 2. When a fraction of graded infill has been prescribed in conjunction with low values of $\rho_{g,max}$, coated structures have been retrieved at the cost of a minor increase in terms of the overall weight. Sandwich structures embedding a self-supporting infill can be effectively exploited in layer-by-layer additive manufacturing to overcome overhang issues. The adoption of passive regions and a proper setting of filters have been tested as simple methods to preserve continuity of the infill, see Example 3 and 4 respectively. Numerical simulations have shown that the type of lattice to be graded remarkably affects the topology of the optimal results, as well as the structural performance in case of load uncertainties. Indeed, shape and locations of the solid features and of the infill have characteristics that are peculiar to the adopted porous microstructure.

It is finally remarked that the proposed method may be straightforwardly applied to constraints on the stress field arising in any linear elastic structure under the effect of probabilistic loading. The ongoing research is mainly involved in stating and testing equivalent deterministic local strength enforcements to deal with uncertainty in loading amplitude, see in particular [23].

## CRediT authorship contribution statement

**Matteo Bruggi:** Conceptualization, Methodology, Software. **Hussein Ismail:** Formal Analysis, Investigation, Data curation. **János Lógó:** Conceptualization, Resources.

## Declaration of competing interest

The authors declare that they have no known competing financial interests or personal relationships that could have appeared to influence the work reported in this paper.

## Data availability

No unreferenced data are required. To facilitate replication of results, the manuscript discusses the formulation in detail and provides the input parameters used to run the numerical examples.

## Acknowledgments

The authors wish to thank the National Research, Development and Innovation Office of Hungary (grant K 138615).

## References

[1] Bendsøe MP, Kikuchi N. Generating optimal topologies in structural design using a homogenization method. Comput Methods Appl Mech Engrg 1988;71(2):197–224.
[2] Bendsøe MP, Sigmund O. Topology optimization: theory, methods and applications. Berlin: Springer; 2003.
[3] Bendsøe MP, Sigmund O. Material interpolation schemes in topology optimization. Arch Appl Mech 1999;69(9–10):635–54.
[4] Eschenauer HA, Olhoff N. Topology optimization of continuum structures: A review. Appl Mech Rev 2001;54(4):331–90.
[5] Wu J, Sigmund O, Groen JP. Topology optimization of multi-scale structures: A review. Struct Multidiscip Opt 2021;63(3):1455–80.
[6] Groen JP, Sigmund O. Homogenization-based topology optimization for high-resolution manufacturable microstructures. Int J Numer Methods Eng 2018;113(8):1148–63.
[7] Allaire G, Geoffroy-Donders P, Pantz O. Topology optimization of modulated and oriented periodic microstructures by the homogenization method. Comput Math Appl 2019;78(7):2197–229.
[8] Xu L, Qian Z. Topology optimization and de-homogenization of graded lattice structures based on asymptotic homogenization. Compos Struct 2021;277.
[9] Jung T, Lee J, Nomura T, Dede EM. Inverse design of three-dimensional fiber reinforced composites with spatially-varying fiber size and orientation using multiscale topology optimization. Compos Struct 2022;279.
[10] Sivapuram R, Dunning PD, Kim HA. Simultaneous material and structural optimization by multiscale topology optimization. Struct Multidiscip Opt 2016;54(5):1267–81.
[11] Hoang V-, Tran P, Vu V-, Nguyen-Xuan H. Design of lattice structures with direct multiscale topology optimization. Compos Struct 2020;252.
[12] Hu J, Luo Y, Liu S. Two-scale concurrent topology optimization method of hierarchical structures with self-connected multiple lattice-material domains. Compos Struct 2021;272.
[13] Gao J, Luo Z, Li H, Li P, Gao L. Dynamic multiscale topology optimization for multi-regional micro-structured cellular composites. Compos Struct 2019;211:401–17.
[14] Li Q, Xu R, Liu J, Liu S, Zhang S. Topology optimization design of multi-scale structures with alterable microstructural length-width ratios. Compos Struct 2019;230.
[15] Xu M, Xia L, Wang S, Liu L, Xie X. An isogeometric approach to topology optimization of spatially graded hierarchical structures. Compos Struct 2019;225.
[16] Guedes J, Kikuchi N. Preprocessing and postprocessing for materials based on the homogenization method with adaptive finite element methods. Comput Methods Appl Mech Engrg 1990;83(2):143–98.
[17] Bensoussan A, Lions JL, Papanicolaou G. Asymptotic analysis for periodic structures. New York: North-Holland; 1978.
[18] Panesar A, Abdi M, Hickman D, Ashcroft I. Strategies for functionally graded lattice structures derived using topology optimisation for additive manufacturing. Addit Manuf 2018;19:81–94.
[19] Casalotti A, D'Annibale F, Rosi G. Multi-scale design of an architected composite structure with optimized graded properties. Compos Struct 2020;252.
[20] Liu J, Gaynor AT, Chen S, Kang Z, Suresh K, Takezawa A, et al. Current and future trends in topology optimization for additive manufacturing. Struct Multidiscip Opt 2018;57(6):2457–83.
[21] Plocher J, Panesar A. Review on design and structural optimisation in additive manufacturing: Towards next-generation lightweight structures. Mater Des 2019;183.
[22] Meng L, Zhang W, Quan D, Shi G, Tang L, Hou Y, et al. From topology optimization design to additive manufacturing: Today's success and tomorrow's roadmap. Arch Comput Methods Eng 2020;27(3):805–30.
[23] Cheng L, Bai J, To AC. Functionally graded lattice structure topology optimization for the design of additive manufactured components with stress constraints. Comput Methods Appl Mech Engrg 2019;344:334–59.
[24] Fu J, Li H, Gao L, Xiao M. Design of shell-infill structures by a multiscale level set topology optimization method. Comput Struct 2019;212:162–72.
[25] Clausen A, Aage N, Sigmund O. Topology optimization of coated structures and material interface problems. Comput Methods Appl Mech Engrg 2015;290:524–41.
[26] Harvey D, Hubert P. Extensions of the coating approach for topology optimization of composite sandwich structures. Compos Struct 2020;252.
[27] Wadbro E, Niu B. Multiscale design for additive manufactured structures with solid coating and periodic infill pattern. Comput Methods Appl Mech Engrg 2019;357.
[28] Yi B, Yoon GH, Peng X. A simple density filter for the topology optimization of coated structures. Eng Optim 2021;53(12):2088–107.
[29] Allaire G, Dapogny C, Estevez R, Faure A, Michailidis G. Structural optimization under overhang constraints imposed by additive manufacturing technologies. J Comput Phys 2017;351:295–328.
[30] Wu J, Wang CCL, Zhang X, Westermann R. Self-supporting rhombic infill structures for additive manufacturing. CAD Comput Aided Des 2016;80:32–42.
[31] Ben-Tal A, Nemirovski A. Robust truss topology design via semidefinite programming. SIAM J Optim 1997;7(4):991–1016.
[32] Marti K. Stochastic optimization methods. Berlin: Springer–Verlag; 2005.
[33] Schuëller GI, Jensen HA. Computational methods in optimization considering uncertainties - An overview. Comput Methods Appl Mech Engrg 2008;198(1):2–13.
[34] da Silva GA, Beck AT. Reliability-based topology optimization of continuum structures subject to local stress constraints. Struct Multidiscip Opt 2018;57(6):2339–55.
[35] da Silva GA, Cardoso EL. Stress-based topology optimization of continuum structures under uncertainties. Comput Methods Appl Mech Engrg 2017;313:647–72.
[36] Lógó J. New type of optimality criteria method in case of probabilistic loading conditions. Mech Based Des Struct Mach 2007;35(2):147–62.
[37] Balogh B, Bruggi M, Lógó J. Optimal design accounting for uncertainty in loading amplitudes: A numerical investigation. Mech Based Des Struct Mach 2018;46(5):552–66.
[38] Guest JK, Igusa T. Structural optimization under uncertain loads and nodal locations. Comput Methods Appl Mech Engrg 2008;198(1):116–24.
[39] Kogiso N, Ahn W, Nishiwaki S, Izui K, Yoshimura M. Robust topology optimization for compliant mechanisms considering uncertainty of applied loads. J Adv Mech Des Syst Manuf 2008;2(1):96–107.
[40] Lazarov BS, Schevenels M, Sigmund O. Topology optimization considering material and geometric uncertainties using stochastic collocation methods. Struct Multidiscip Opt 2012;46(4):597–612.
[41] Chun J, Song J, Paulino GH. Structural topology optimization under constraints on instantaneous failure probability. Struct Multidiscip Opt 2016;53(4):773–99.
[42] da Silva GA, Cardoso EL, Beck AT. Non-probabilistic robust continuum topology optimization with stress constraints. Struct Multidiscip Opt 2019;59(4):1181–97.
[43] Csébfalvi A. A new theoretical approach for robust truss optimization with uncertain load directions. Mech Based Des Struct Mach 2014;42(4):442–53.
[44] Zheng Y, Da D, Li H, Xiao M, Gao L. Robust topology optimization for multi-material structures under interval uncertainty. Appl Math Model 2020;78:627–47.
[45] Gao X, Chen W, Li Y, Chen G. Robust topology optimization of multi-material structures under load uncertainty using the alternating active-phase method. Compos Struct 2021;270.
[46] A. Prékopa. Stochastic programming. Budapest, Dordrecht: Akadémia Kiad´ó and Kluwer; 1995.
[47] Vrouwenvelder T. The JCSS probabilistic model code. Struct Saf 1997;19(3):245–51.
[48] Svanberg K. The method of moving asymptotes-A new method for structural optimization. Int J Numer Methods Eng 1987;24(2):359–73.
[49] Khot NS, Berke L, Venkayya VB. Comparison of optimality criteria algorithms for minimum weight design of structures. AIAA J 1979;17(2):182–90.
[50] Sigmund O, Torquato S. Design of materials with extreme thermal expansion using a three-phase topology optimization method. J Mech Phys Solids 1997;45(6):1037–67.
[51] Stegmann J, Lund E. Discrete material optimization of general composite shell structures. Int J Numer Methods Eng 2005;62(14):2009–27.
[52] Ferrari F, Sigmund O. A new generation 99 line Matlab code for compliance topology optimization and its extension to 3D. Struct Multidiscip Opt 2020;62(4):2211–28.
[53] Hassani B, Hinton E. A review of homogenization and topology optimization I - Homogenization theory for media with periodic structure. Comput Struct 1998;69(6):707–17.
[54] Andreassen E, Andreasen CS. How to determine composite material properties using numerical homogenization. Comput Mater Sci 2014;83:488–95.
[55] Day AR, Snyder KA, Garboczi EJ, Thorpe MF. The elastic moduli of a sheet containing circular holes. J Mech Phys Solids 1992;40(5):1031–51.

[56] Kumar RS, McDowell DL. Generalized continuum modeling of 2-D periodic cellular solids. Int J Solids Struct 2004;41(26):7399–422.
[57] Kaw K. Mechanics of composite materials. Boca Raton: CRC Press; 2006.
[58] Bruggi M, Laghi V, Trombetti T. Simultaneous design of the topology and the build orientation of wire-and-arc additively manufactured structural elements. Comput Struct 2021;242.
[59] Borrvall T, Petersson J. Topology optimization using regularized intermediate density control. Comput Methods Appl Mech Engrg 2001;190(37–38):4911–28.
[60] Bourdin B. Filters in topology optimization. Int J Numer Methods Eng 2001;50(9):2143–58.
[61] Wang F, Lazarov BS, Sigmund O. On projection methods, convergence and robust formulations in topology optimization. Struct Multidiscip Opt 2011;43(6):767–84.
[62] Guest JK, Prévost JH, Belytschko T. Achieving minimum length scale in topology optimization using nodal design variables and projection functions. Int J Numer Methods Eng 2004;61(2):238–54.
[63] Kawamoto A, Matsumori T, Yamasaki S, Nomura T, Kondoh T, Nishiwaki S. Heaviside projection based topology optimization by a PDE-filtered scalar function. Struct Multidiscip Opt 2011;44(1):19–24.
[64] Pasini D, Guest JK. Imperfect architected materials: Mechanics and topology optimization. MRS Bull 2019;44(10):766–72.
[65] Chen Y, Peng X, Kong L, Dong G, Remani A, Leach R. Defect inspection technologies for additive manufacturing. Int J Extreme Manuf 2021;3(2).
[66] Nazir A, Abate KM, Kumar A, Jeng J-. A state-of-the-art review on types, design, optimization, and additive manufacturing of cellular structures. Int J Adv Manuf Technol 2019;104(9–12):3489–510.
[67] Aage N, Andreassen E, Lazarov BS. Topology optimization using PETSc: An easy-to-use, fully parallel, open source topology optimization framework. Struct Multidiscip Opt 2015;51(3):565–72.
[68] Achtziger W. Topology optimization of discrete structures. In: Topology optimization in structural mechanics. Rozvany GIN Ed.. Vienna: Springer; 1997.
[69] Sigmund O, Aage N, Andreassen E. On the (non-)optimality of Michell structures. Struct Multidiscip Opt 2016;54(2):361–73.
[70] Bendsøe MP. Optimal shape design as a material distribution problem. Struct Opt 1989;1:193–202.